Journal of Biomedical Optics

SPIEDigitalLibrary.org/jbo

Extended scan depth optical coherence tomography for evaluating ocular surface shape

Meixiao Shen
Lele Cui
Ming Li
Dexi Zhu
Michael R. Wang
Jianhua Wang

SPIE

Extended scan depth optical coherence tomography for evaluating ocular surface shape

Meixiao Shen,[a] Lele Cui,[a,c] Ming Li,[a,c] Dexi Zhu,[a,c] Michael R. Wang,[b] and Jianhua Wang[a]
[a]University of Miami, Bascom Palmer Eye Institute, Department of Ophthalmology, 1638 NW 10th Avenue, Miami, Florida 33136
[b]University of Miami, Electrical and Computer Engineering, 1251Memorial Drive, Coral Gables, Florida 33146
[c]Wenzhou Medical College, School of Optometry and Ophthalmology, 270 Xueyuan Road, Wenzhou 325027, China

Abstract. Spectral domain optical coherence tomography (SD-OCT) with extended scan depth makes it possible for quantitative measurement of the entire ocular surface shape. We proposed a novel method for ocular surface shape measurement using a custom-built anterior segment SD-OCT, which will serve on the contact lens fitting. A crosshair alignment system was applied to reduce the misalignment and tilting of the eye. An algorithm was developed to automatically segment the ocular surface. We also described the correction of the image distortion from the segmented dataset induced by the nontelecentric scanning system and tested the accuracy and repeatability. The results showed high accuracy of SD-OCT in measuring a bicurved test surface with a maximum height error of 17.4 μm. The repeatability of *in vivo* measurement was also good. The standard deviations of the height measurement within a 14-mm wide range were all less than 35 μm. This work demonstrates the feasibility of using extended depth SD-OCT to perform noninvasive evaluation of the ocular surface shape. [DOI: 10.1117/1.3578461]

Keywords: optical coherence tomography; ocular surface.

Paper 10557R received Oct. 13, 2010; revised manuscript received Feb. 22, 2011; accepted for publication Mar. 24, 2011; published online May 10, 2011.

1 Introduction

An imaging technique that could quantitatively evaluate the ocular surface shape beyond the limbus would be beneficial for evaluating contact lens fitting and design,[1–3] monitoring corneal changes,[4] and screening refractive surgery candidates.[5] In the field of contact lens fitting, the ocular surface shape is the main factor that impacts the fitting for a given lens.[6] For rigid lenses, the movement, centration, and stability depend on the shape of the peripheral cornea. For soft lenses, the fit depends on the shape of the limbus and sclera as well as the peripheral cornea rather than the central corneal curvature.[3,7] Therefore, knowledge of the peripheral corneal and scleral topography may help to understand the interaction of the contact lens with the ocular surface, and thus help choose a suitable lens design for a given ocular surface shape. This in turn may reduce or eliminate lens-related sight-threatening complications. Several commercial imaging modalities are capable of providing shape information for the ocular surface. These devices include slit scanning topography,[8] ultrasound biomicroscopy,[9] Scheimpflug imaging,[10,11] and placido ring-based systems.[12] However, these methods are either limited to evaluating only the central cornea or just providing images with low sampling density due to insufficient acquisition speed.

Optical coherence tomography (OCT) is a powerful imaging technique for *in vivo* detection of tissue microstructure with high resolution.[13] It can be used to capture a cross sectional or three dimensional volume images.[6,14–20] Compared with conventional time domain OCT, Fourier domain OCT (FD-OCT) offers significant advantages in imaging speed and sensitivity.[21,22] There are two primary types of FD-OCT implementations, depending on the light source and detector configuration. One is the spectral domain OCT (SD-OCT) with a spectrometer and a line-scan charge-coupled device (CCD). The other is the swept light source OCT (SS-OCT) that employs a wavelength tunable laser source and a single detector. Both SD-OCT and SS-OCT have been widely applied in the ophthalmic imaging of the posterior and anterior segments.[6,16,17,19,20] Compared with SS-OCT, SD-OCT has the advantage of higher resolution and increased phase stability for functional imaging.[23]

Despite rapid advances in SD-OCT, the limited imaging range due to finite resolution of spectrometer remains a major drawback. Unlike the retina, ocular surface shape measurement requires deep scan depth and large scan width to cover the cornea and scleral zone, so that the complete corneal-scleral junction can be seen. The depth of the anterior segment is more than 3 mm measured from the apex of the cornea to the anterior surface of the crystalline lens. The diameter is about more than 12 mm up to the scleral zone. There is a depth-dependent loss of sensitivity in SD-OCT due to washout of interferogram fringe visibility with increasing imaging depth. This loss limits the application of anterior segment SD-OCT to only shallow depth imaging. Due to the large slope of the ocular surface, this drawback causes a decrease in signal-to-noise ratio (SNR) from the corneal apex to the sclera. Several approaches have been proposed to overcome this problem, such as phase shift techniques,[17,24,25] an optical frequency comb with additional tunable fiber Fabry-Perot interferometer,[26] and a spectrometer with special custom design.[27]

Address all correspondence to: Jianhua Wang, University of Miami, Bascom Palmer Eye Institute, Miller School of Medicine, 1638 NW 10th Avenue, McKnight Building - Room 202A, Miami, Florida 33136. Tel: 305 482 5010; Fax: 305 482 5011; E-mail: jwang3@med.miami.edu.

1083-3668/2011/16(5)/056007/10/$25.00 © 2011 SPIE

Recently, OCT has been used to quantitatively measure the biometry of the anterior ocular segment.[28–31] We have now developed a new custom-built SD-OCT with extended scan depth to measure the ocular surface shape and enable the evaluation of contact lens fitting. This instrument can image the entire ocular surface, including the cornea, limbus, and sclera. Quantitative measurement of the ocular surface, especially the peripheral cornea at the corneal-scleral junction, will provide more information for rigid and soft contact lens fitting, which in turn may lead to improvements in lens design. There are several unique difficulties to overcome when the SD-OCT is used to measure the ocular surface shape. The first is to control the misalignment and tilt of the corneal surface that are present, which may influence the repeatability of topographic analyses. The second difficulty is to correct the image distortion induced by the nontelecentric scanning system. Anterior segment OCT scanners described to date utilize a nominally telecentric scanning geometry that consists of mutually parallel A-scans that are normal to the corneal surface at its apex.[32,33] The possibility of introducing fast optical scanners makes OCT a perfect tool to act as a topographer. However, due to small optical misalignments and aberrations in real scanners, even small departures from this ideal may detract from the stringent accuracy required for ocular shape. The last difficulty is to develop an automated image processing method to analyze the ocular surface shape. Due to the SNR loss with the increasing imaging depth, a robust algorithm is necessary for automated image processing.

In this paper, we describe a method for ocular surface shape measurement using the anterior segment SD-OCT with extended scan depth. A crosshair alignment system was employed to reduce the misalignment and tilt of the eye. We also developed algorithms for automated segmentation of the ocular surface and correction of image distortion induced by the nontelecentric scanning system. The accuracy and repeatability for this SD-OCT instrument to measure the surface dimensions were tested *in vitro* and *in vivo*.

2 Materials and Methods

2.1 *Extended Scan Depth SD-OCT*

The schematic of the system setup used for ocular surface shape measurement is illustrated in Fig. 1. A light from the superluminescent diode source (InPhenix, IPSDD0808, Livermore, California) with a center wavelength of 840 nm and a full width at half maximum bandwidth of 45 nm was split into a reference and a sample arm by a 50:50 fiber coupler. The reference light was delivered to a silver mirror by a collimating lens and an objective lens. In the sample arm, a collimating lens ($f = 11$ mm) was used to deliver the light into the sample. The power delivered to the sample was 1.2 mW. An *x-y* galvanometer pair was used to provide the B scan. The light was focused on the sample by an objective lens ($f = 100$ mm), which gave ~20 μm lateral resolution. The backscattered light from the two arms was recombined by the fiber coupler and collimated by an 11 mm focal length collimator. It then entered a custom-designed spectrometer comprised of a diffraction grating (1800 lp/mm volume holographic grating), an achromatic lens ($f = 150$ mm), and a line scan CCD camera (Aviiva SM2 CL 2010 by e2v, 12-bit, 2048 pixels, pitch 10 μm, San Jose, California).

Figure 2(a) shows the spectrum of the light source captured by this OCT system. The calculated spectral resolution was 0.024 nm, corresponding to a detectable depth range of 7.3 mm in air. Figure 2(b) shows a zoomed point spread function, measured at $z = 0.52$ mm (z, imaging depth). The calculated axial resolution of the OCT system for 2048 pixels was 10.4 μm in air and ~7.5 μm in tissue. The A-line (depth scan) rate of the OCT system was set at 24 kHz. Under these operating conditions, the sensitivity was about 107 dB near the

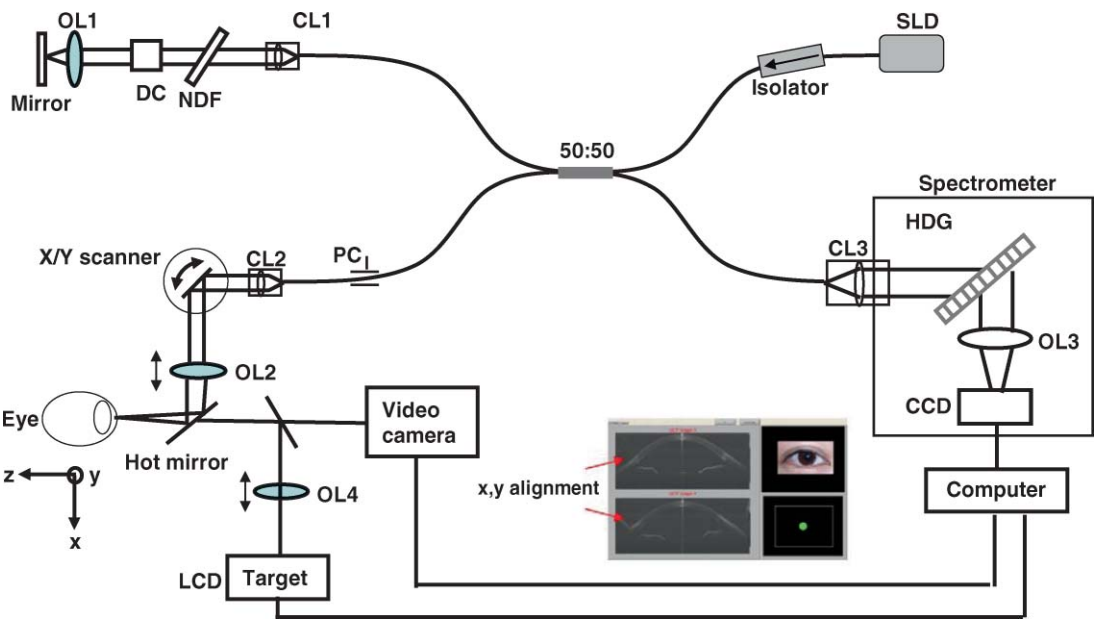

Fig. 1 Experimental SD-OCT setup: SLD – superluminescent diode, PC – polarization controller, NDF – neutral density filter, DC – dispersion compensator, CL1-CL3 – Collimating lenses, OL1-OL4 – objective lenses, HDG – holographic volume diffraction grating, CCD – line scan camera.

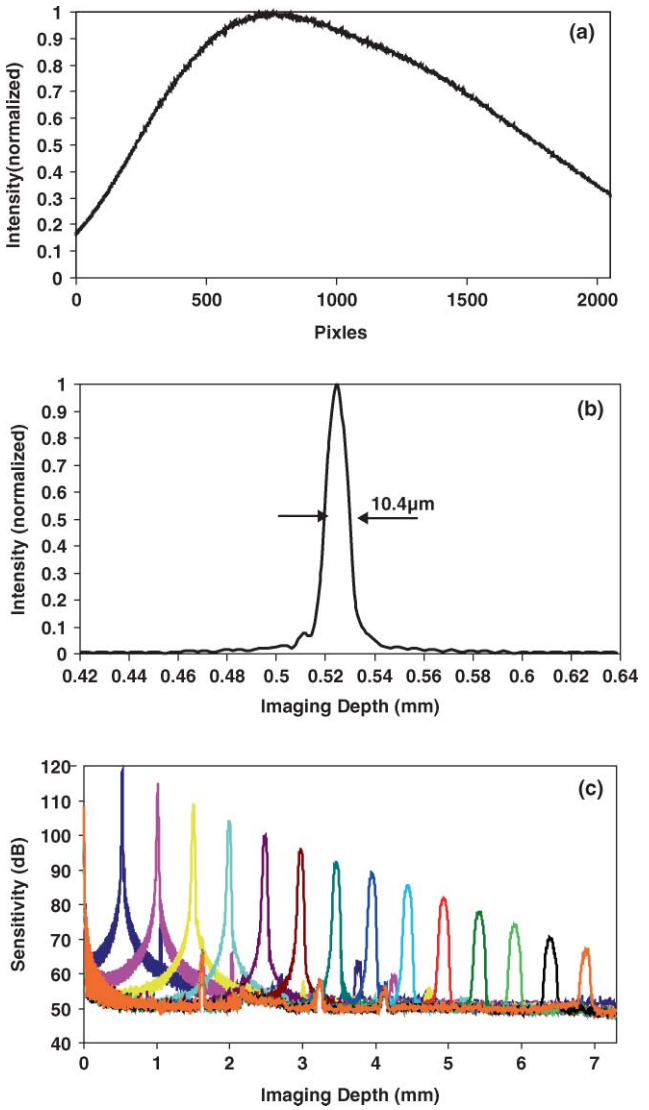

Fig. 2 (a) Spectrum of the light source captured by the spectrometer of the SD-OCT system. (b) Point spread function of the axial resolution according to the spectrum full bandwidth the spectrometer detected. The measured axial resolution was 10.4 μm in air. (c) Measured sensitivity roll off versus the imaging depth. The sensitivity was obtained with a partial reflector with -40 dB reflectivity and all the curves were obtained by averaging over 100 consecutive measurements.

zero-delay plane. Figure 2(c) shows the measured loss of sensitivity versus the imaging depth z. The sensitivity gradually becomes reduced to 97 dB at the imaging depth of 5 mm. The image width and number of A-scans in each B-scan were adjustable but set to a width of 18 mm and 2048 pixels for ocular surface imaging.

A telecentric-designed optical scanning probe (sample arm) allowing a scan width up to 20 mm was mounted on a modified slit lamp with a video camera for aiming. Customized software was developed to simultaneously control the horizontal and vertical scans, and the images were simultaneously viewed in the operation window of the instrument (inset of Fig. 1). *X-Y* cross aiming allowed alignment of the scanning position through the iris and corneal apex during imaging. An internal fixation target controlled by a computer was displayed on a miniature liquid crystal display monitor. Moving this internal fixation target guided the subject's eye to fix at one direction.

2.2 *Experiment*

We performed three experiments with the extended scan depth SD-OCT to evaluate the accuracy and repeatability of the technique to measure the ocular shape. *In vitro* samples included a mirror with a flat optical surface and a custom-made bicurved test surface. Eight subjects (8 eyes) were recruited for *in vivo* measurements. The study was approved by the review board at the University of Miami and adhered to the tenets set forth in the Declaration of Helsinki. Informed consent was obtained from each subject. All *in vitro* samples and *in vivo* human eyes were imaged with the 18 mm scan width.

The scanning system of the probe was calibrated by imaging a mirror with a flat optical surface. The accuracy was tested on a custom-made 18-mm diameter, bicurved test surface that simulated the ocular surface shape in which the corneal and scleral curvatures are different from one another. The central 10-mm region was steeply curved (radius = 8.1 mm), and then it quickly transitioned to a flatter peripheral curvature (radius = 12.0 mm). A Talysurf instrument with a resolution of 16 nm (Taylor Hobson Inc., Rolling Meadows, Illinois) was used to accurately quantify the height profile of the test surface. The measurements taken by the SD-OCT instrument after correction for fan distortion were then compared with the results from the Talysurf.

The repeatability of the method was tested on *in vivo* measurements of human ocular surfaces. All measurements were repeated two times. Each subject was asked to sit in front of the slit lamp and look at the fixation target. The subject was guided to move the eye during the alignment. The image was acquired when the iris was horizontal in the OCT scan and the corneal apex was centered in both the horizontal and vertical scans. After image acquirement, the subject was asked to sit back while the fixation target was misaligned. After several minutes, the same procedure was repeated and alignment was re-established by adjusting the fixation target. SD-OCT images were taken on both thr horizontal and vertical meridians.

3 Image Analysis

Figure 3 shows the typical extended scan depth SD-OCT raw images of a subject who was able to widely open his eyes. The coverage was up to 18 mm in the horizontal and 16 mm in the vertical meridians. The 2-dimensional cross section scans (B-scans) consisted of 2048 line scans (A-scans), with 2048 points per A-scan. The measurement time for one B-scan image is about 83 ms. The light penetration was sufficient to image the entire ocular surface and clearly visualize the limbus and the junction between cornea and sclera, although the SNR was reduced around the sclera compared to the cornea. We developed an algorithm using Matlab language (Matlab, Natick, Massachusetts) to automatically analyze the SD-OCT images and extract the surface shape information.

Three main steps were automatically performed to yield parameters describing the ocular surface: 1. segmenting the ocular surface in the original SD-OCT image to yield the coordinates of the surface, 2. correcting the image distortion induced by

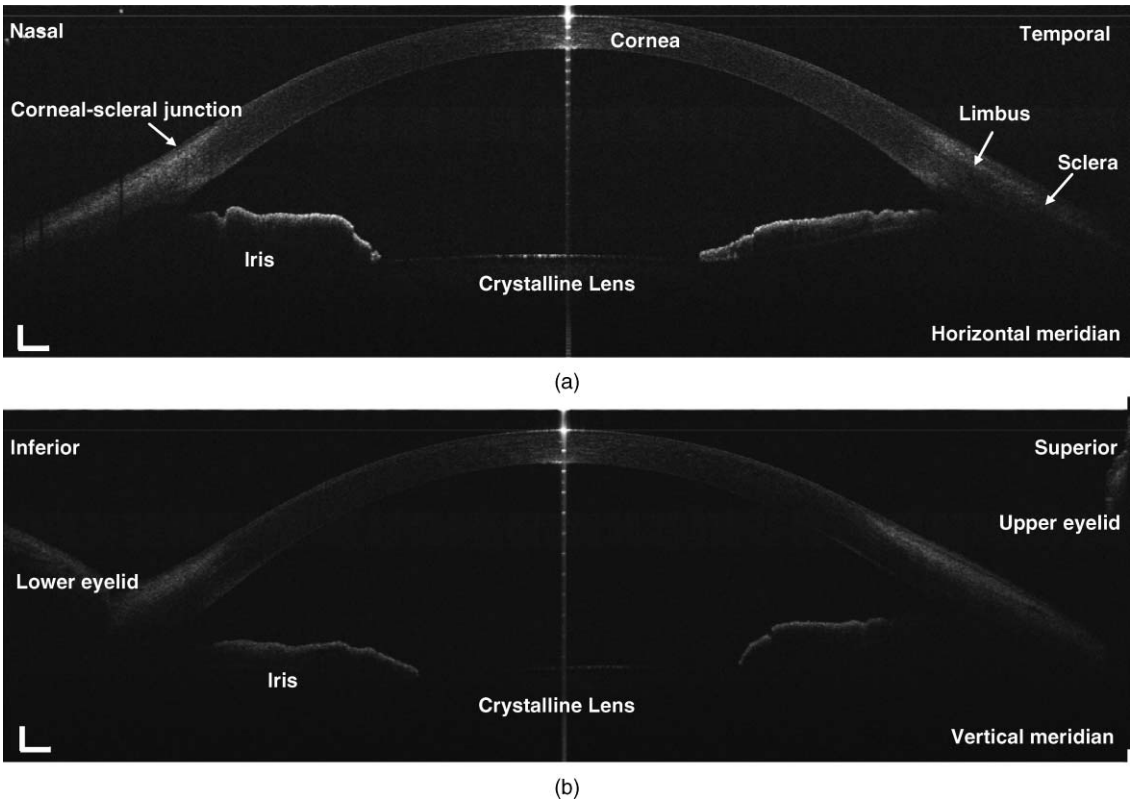

Fig. 3 Original anterior segment images acquired by the extended scan depth SD-OCT. The full scan width was 18 mm and the scan depth was 7.3 mm. (a) Image acquired in the horizontal meridian. (b) Image acquired in the vertical meridian. Bar = 500 μm.

the non-telecentricity in the scanning system, and 3. calculating the surface measurements, including the sagittal height and curvature. Figure 4 shows the main steps of the algorithm to automatically segment the boundary of the ocular surface and obtain the shape parameters on OCT images.

3.1 *Automatic Segmentation*

Preprocessing was performed to reduce background noise. Most of the background noises in 840 nm SD-OCT images come from the camera. To reduce the background noise and provide a much cleaner result for the following process steps, a median filter and Gaussian filter with a 5×5 kernel were used to remove most of the background noise in the image [Fig. 5(a)].

After background noise reduction, the following five steps were performed by the algorithm to locate the boundary of the ocular surface: 1. applying the threshold to create a mask, 2. processing the mask using binary morphology, 3. calculating the gradient image over the preprocessed image, 4. masking the gradient image and searching the first local maximum gradient locations, and 5. refining the boundary.

Traditionally, a threshold was located and directly applied on a gray-level image to obtain the binary image using a global thresholding technique, such as Otsu's method.[34] However, this method was not suitable for all current SD-OCT images due to the variations in the SNR. Due to the different features of the texture between the entire ocular surface and the other structures, such as the iris, prior to finding a threshold, we used an entropy filter[35] to improve the robustness of the algorithm. This texture analysis approach has been shown to work well on the contact lenses OCT images.[36] The process created an entropy map. Based on the entropy map, Otsu's method[34] was applied to obtain an ideal global threshold and then a binary image was created. After that, a series of morphological operations, such as an operation for removing the small objects and filling of the

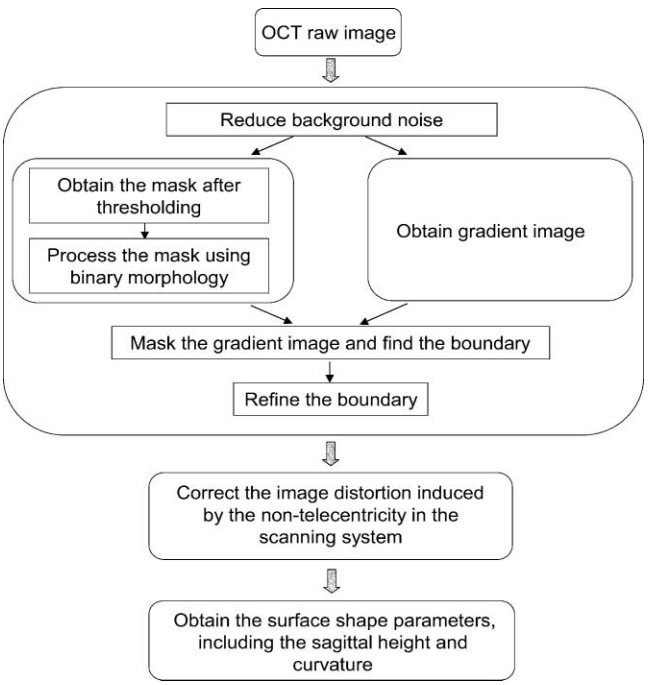

Fig. 4 Flowchart of the algorithm showing the main processing steps that automatically segment the boundary of ocular surface and obtain the shape parameters on OCT images.

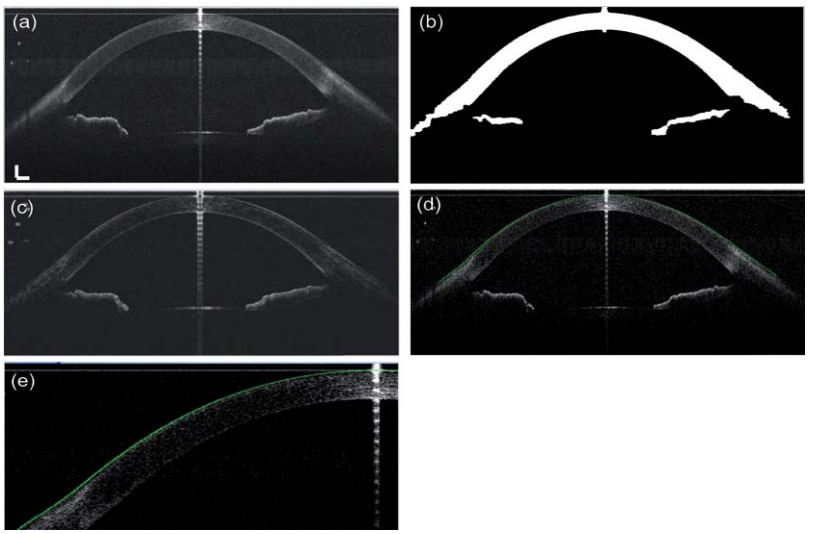

Fig. 5 (a) Image preprocessed by median and Gaussian filters. (b) Mask after threshold on the entropy mask and the operation of the binary morphology. (c) The gradient image that was calculated over the preprocessed image. (d) The ocular surface boundary that was overlaid on the initial OCT image. (e) The enlarged image (d), which shows the good fit of the boundary. Bar = 500 μm.

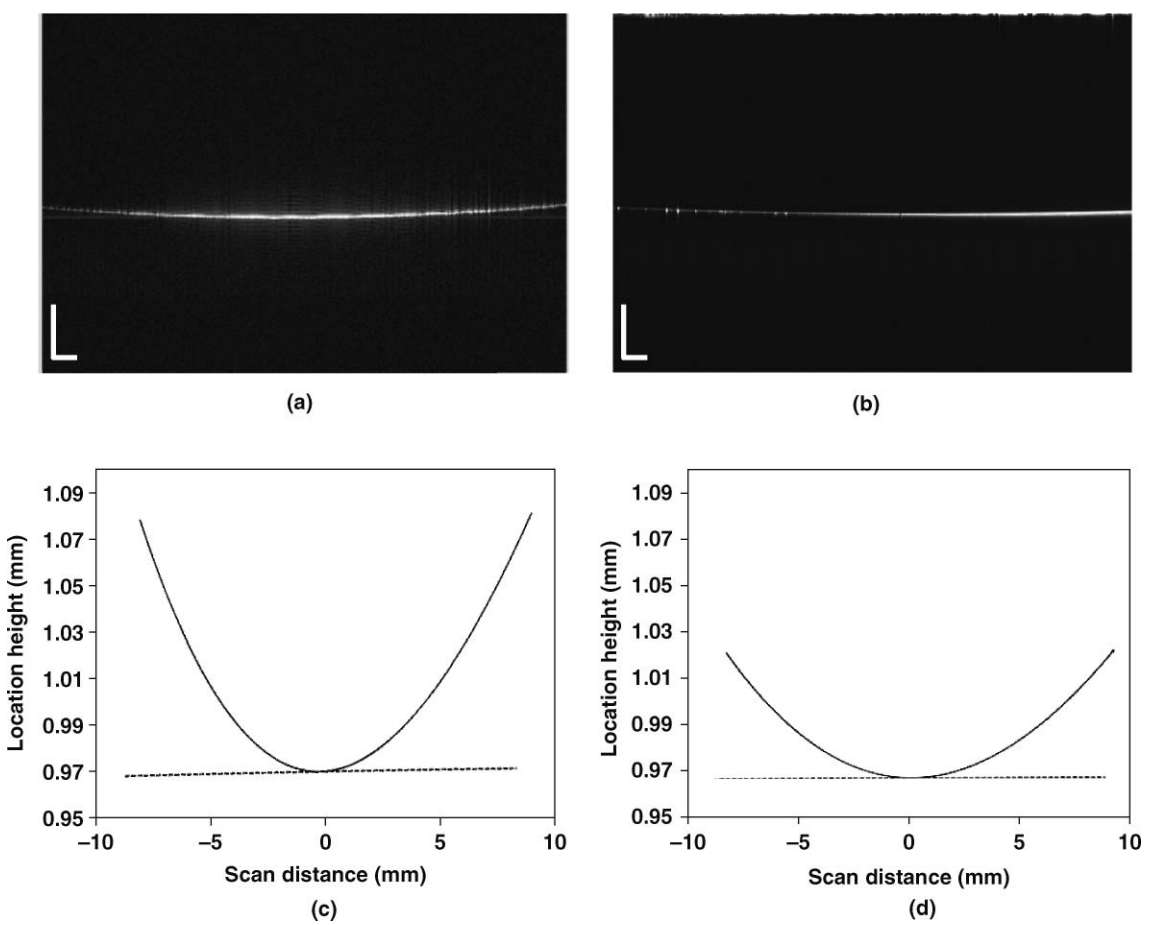

Fig. 6 SD-OCT images of a mirror with a flat optical surface captured in two perpendicular directions and nontelecentric calibration. (a) SD-OCT image captured in horizontal scan. (b) SD-OCT image captured in vertical scan. The least squared curve fitting [solid line in panels (c) and (d)] for the deformed field curvature induced by the nontelecentric illumination was used to obtain the pivot distance. Straight lines both in the (c) horizontal and (d) vertical meridian scans were obtained after the correction (dashed line). Bar = 500 μm.

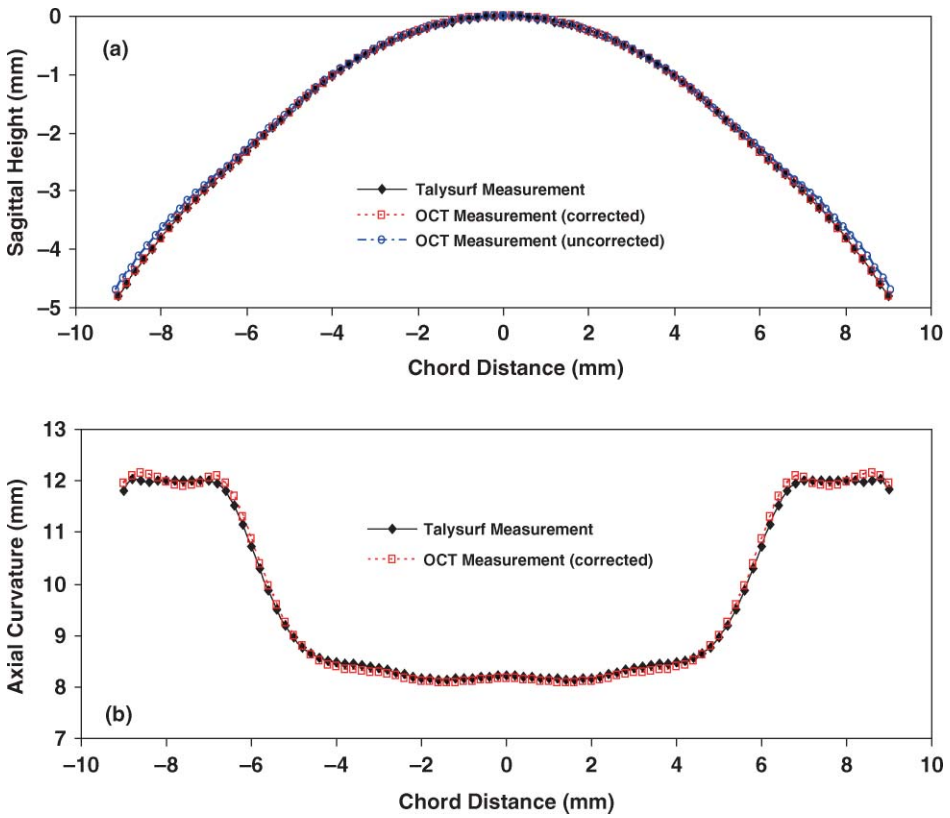

Fig. 7 (a) Height profiles before and after correction for image distortion of the test surface derived from a SD-OCT image. The corrected results compared very well with that determined by the Talysurf instrument. The maximum error between the uncorrected sagittal height measured by SD-OCT and measurement by the Talysurf instrument was 100 μm within the 18 mm chord distance. After correction, this error reduced to 17.4 μm. (b) Comparison of the curvature radius calculated from the corrected OCT height profile and Talysurf measurement.

holes in the corneal and erosion, was performed to generate a mask by retaining the largest white area, while eliminating all others [Fig. 5(b)]. The initial boundary for the ocular surface was obtained based on the mask.

Next, the gradient was calculated based on the preprocessed image and was masked based on the initial ocular surface boundary [Fig. 5(c)]. Once the masked gradient image was created, the algorithm began searching for data points along the boundary of the ocular surface. The first local maximum gradient locations provided the initial boundary for the surface. We assumed that the true edge of the ocular surface existed in the peaks of the outermost speckles in the ocular surface region. The algorithm searched along the detected edge of the mask for the brightest pixel in a small region of 7×7 pixels. This pixel area roughly corresponded with the size of the speckle, where it was assumed that the brightest pixel corresponded with the peak of the speckle. After that, a polynomial fitting with 10th order was then performed to smooth the identified boundary [Figs. 5(d) and 5(e)]. The algorithm deleted unreliable boundary locations due to the bright areas in the cornea apex, axial scans that were shadowed by the eye lash/lid, and corneal boundary locations that could not be connected to those of neighboring axial scans (bumps in the boundary).

3.2 *Correction of the Image Distortion Induced by the Nontelecentric Scanning*

To correct for nontelecentric scanning geometric image distortion effects, we applied the two dimensional nontelecentric correction method in the following equations previously described by Westphal et al.[28]

$$x' = F(x, y) = \arctan\left(\frac{x}{D - y}\right) D, \tag{1}$$

$$y' = F(x, y) = D - \sqrt{x^2 + (D - y)^2}. \tag{2}$$

Here, x' and y' denote the coordinates across and along single depth A-scans in the raw OCT image. The corresponding coordinates x and y were in the corrected image. D was the distance between the center of the field of view and the scanning pivot. Prior to correcting the distortion of the surface shape, D was obtained for the probe in the specific scanning field of view.

3.3 *Calculation of the Ocular Surface Shape*

We applied the tangent curvature (power) of the ocular surface to characterize the shape based on the sagittal height information. The tangent curvature (Ct) was obtained using the thin lens equation $\mathrm{Ct} = 1000(\mathrm{n} - 1)/\mathrm{Rt}$, where n is the simulated keratometric refractive index 1.3375 and Rt is the tangent radius. The unit of curvature is diopter. The tangent curvature described the bending of the ocular surface in a given direction through a given point. The tangent radius (Rt) was defined as

$$Rt = (d^2z/dx^2)^{-1}(1 + (dz/dx)^2)^{3/2}, \tag{3}$$

where z was the sagittal height and x was the coordinate of the chord.[37]

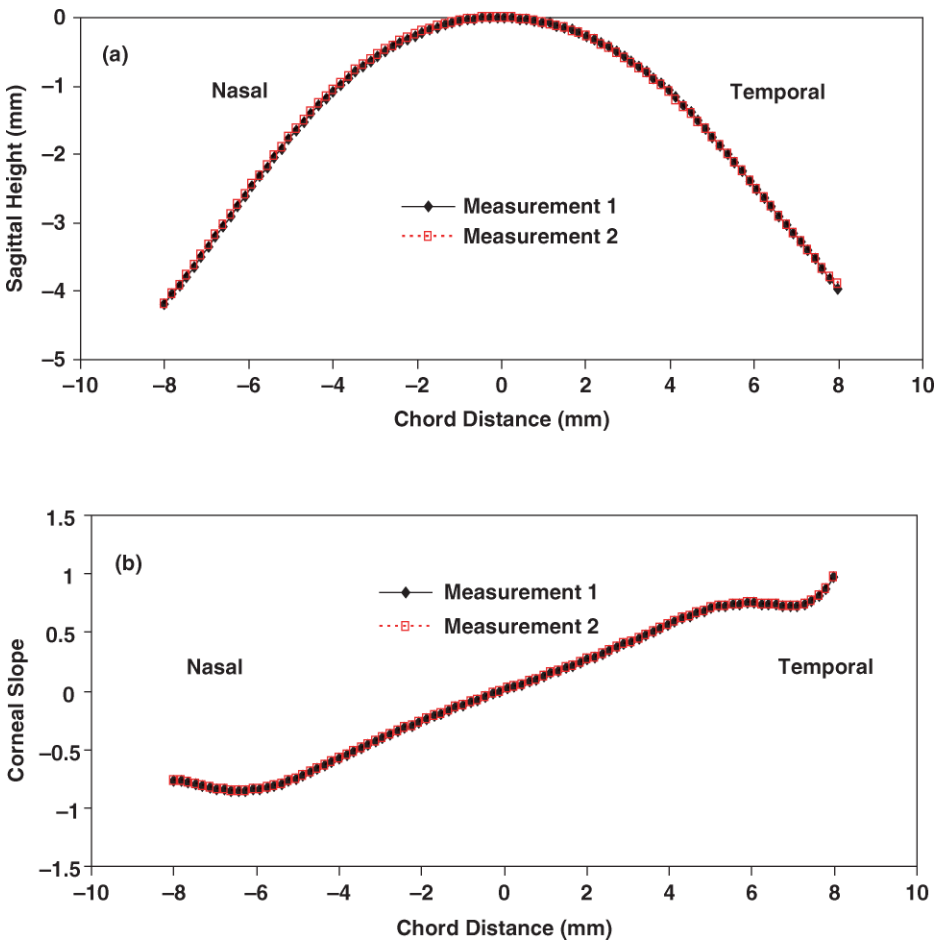

Fig. 8 (a) Replicate sagittal heights of the ocular surface taken at the horizontal meridian for one eye of a subject. The repeatability of the overall sagittal height between two measurements was good. (b) Replicate slopes of the ocular surface in (a). It indicated good repeatability. Measurement 1 is the first measurement and measurement 2 is the second measurement.

4 Results

4.1 *Calibration of the Scanning System*

Figure 6 presents two SD-OCT images of a flat optical mirror surface captured in two perpendicular directions. The edge of the flat surface became curved, and in the horizontal scan, the cross section of the curvature [Fig. 6(a)] was larger than in the perpendicular vertical scan [Fig. 6(b)]. A linear least square circular curve fitting of the field curvature was used to obtain D, as described in previous studies.[28,31] In our system, D was 363.5 mm in the horizontal scan and 584.1 mm in the vertical scan, which was quite close to the ideal telecentric illumination condition. This nontelecentric quantization was used to correct ocular surfaces by employing Eqs. (1) and (2). Figures 6(c) and 6(d) show the effect of the flat surface before and after correction. After correction, a straight line was obtained.

4.2 *Accuracy*

When the sagittal height was plotted against the horizontal scan chord distances of the bicurved test surface, the apex was at the zero point [Fig. 7(a)]. The corrected sagittal height, determined by processing of the SD-OCT images, agreed well with the Talysurf data. Before correction, the maximum sagittal height error between the OCT and Talysurf measurements was up to 100 μm within the 18-mm chord distance. The root mean squared error value for the overall curve fitting between the corrected data of SD-OCT and Talysurf data was 0.14 μm and the largest sagittal height error was reduced to 17.4 μm. In the curvature profile of the bicurved surface calculated from the height profile [Fig. 7(b)], the curvature radius was comparable with the well-defined radius values.

4.3 *Repeatability*

Figure 8(a) shows the repeatability of the overall sagittal height measurement for one eye of a subject taken at the horizontal meridian. When the slopes of the curves were plotted against the chord distance, regions with increasing heights had positive slopes [Fig. 8(b)]. Both results indicated good repeatability between the two measurements. The repeatability of the measurements *in vivo* human eyes are listed in Table 1. The standard deviations of the differences between two repeated measurements within a 14-mm wide range were all less than 35 μm. The repeatability in the center zone was better than that in the peripheral region.

4.4 *Curvature Profiles of Ocular Surface*

Figure 9 shows the tangent curvature profiles in the horizontal [Fig. 9(a)] and vertical meridians [Fig. 9(b)] derived from Eq. (3). They showed that this eye had a negative curvature in

Table 1 Repeatability (standard deviation of the difference between two repeated measurements, μm) of SD-OCT to measure the sagittal height of human ocular surface ($n = 8$ eyes). *L3, L4, L5, L6, and L7 are chord distances of 3, 4, 5, 6, and 7 mm from the corneal apex, respectively.

	Horizontal meridian		Vertical meridian	
Location*	Nasal	Temporal	Inferior	Superior
L3	±17.5	±24.2	±20.7	±11.1
L4	±17.3	±29.6	±29.6	±15.4
L5	±19.1	±31.8	±32.2	±23.0
L6	±22.2	±32.4	±33.9	±30.8
L7	±22.0	±32.3	±31.8	±20.9

the limbal region that was apparent in the horizontal and vertical raw images [Figs. 9(c) and 9(d)]. The locations with the maximum negative curvatures corresponded to the corneal-scleral junction angle.

5 Discussion

The custom-built SD-OCT with extended scan depth and 18 mm width of coverage imaged the entire ocular surface. The developed algorithms processed, segmented, and corrected image distortion due to the nontelecentric scanning system without the need for user input. Cross-hair alignment was applied to reduce the misalignment prior to image capture. This method may become a promising tool for the fitting of contact lenses with larger diameters.

Automated segmentation of the SD-OCT images makes it possible to evaluate the ocular surface, both qualitatively and quantitatively. This demonstrates satisfying robustness in OCT image acquirement and processing. The key requirement for obtaining the ocular surface height information was to accurately locate the ocular surface. The texture-based thresholding technique used for segmentation proved to be a reliable way of initially locating the ocular surface in the image. Based on the assumptions that the ocular surface is smooth and lies along the first peak on each A-line, the algorithm estimated the location of the ocular surface with pixel precision. Visual inspection revealed that the lines drawn by the software to mark the locations of the ocular surfaces were in fact directly located on the peak of each A-line.

Nontelecentric scanning can contribute error to quantitative OCT measurements, especially for the wide scan width.[38,39] In the present study, the probe system was calibrated and it presented a detectable curvature in the SD-OCT image caused by lack of telecentricity of the scanning system when imaging a flat surface. In the algorithm, we added the telecentricity corrections to the image based on the equations provided by Westphal et al.[28] After correction, the edge of the flat surface should be a straight line in the image, an assumption that we validated. The measurements of the bicurved model of the ocular surface indicated that the maximum sagittal height error measured by SD-OCT was reduced to 17.4 μm from 100 μm before correction. This implies that our OCT method has enough accuracy to measure the surface shape of a stationary object.

Our tests indicated that the extended depth scan SD-OCT system had good repeatability for ocular surface measurements. The standard deviations of the height measurements up to 14 mm wide were all less than 35 μm. This precision is also enough for contact lens fitting. Prior to image capture, *X-Y* crosshair alignment was applied as a guide. Without the *X-Y* crosshair alignment, there was a substantial misalignment and tilting of the eye. When we only used the scanning on one meridian,

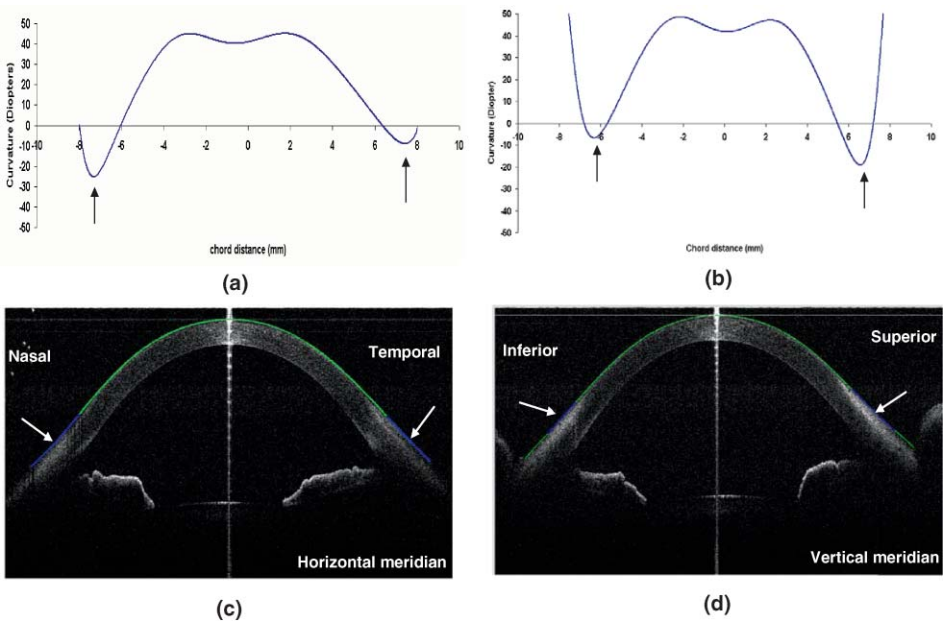

Fig. 9 Curvature profiles of the ocular surface for the left eye of one subject. (a) Horizontal meridian. (b) Vertical meridian. (c) The fitted boundary overlaid on the SD-OCT image acquired in the horizontal meridian. (d) The fitted boundary overlaid on the SD-OCT image acquired in the vertical meridian. Green lines, positive curvature; Blue lines, negative curvature; Arrows, junction angles. Bar = 500 μm. (Color online only.)

misalignment occurred almost every time, which indicates the importance of using the *X-Y* cross application in OCT scanning of the ocular surface. The ocular surface information with 14 mm coverage should be sufficient for evaluating contact lens fitting. Measurements such as sagittal height, corneal curvature, and peripheral shape around the corneal-scleral junction can be estimated based on the height information, which may be the key factor that affects the lens fit. Furthermore, this technique is noninvasive and nondestructive, which makes it suitable for precise quantization of the ocular surface and its interaction with the contact lens.

The measurement had poor precision in the peripheral region compared to the central cornea. There are several reasons for this. The main reason is the SNR drop in the limbal-scleral regions. In SD-OCT images, there is a zero-delay line at which the real image overlaps the mirror image. During imaging, the ocular surface was located below the zero-delay line to avoid the overlap. However, there is a loss of sensitivity with increased distance from the zero-delay line.[16,40,41] In our present method, the SD-OCT system had 10 dB loss of sensitivity at limbal-scleral regions (about 5 mm imaging depth). So the SNR around this area is much lower compared to the central region of the cornea. The decreased SNR may impact the detection of the true location of the surface, thus affecting the precision of measurement. Some methods can improve the SNR in the scleral regions, such as phase-shift technology.[17,24] Using a camera with higher number of pixels, for example, a COMS (complementary metal oxide semiconductor) camera with 4096 pixels (Basler Sprint camera), could also improve the sensitivity roll-off performance.[25] The other reason for poor repeatability is eye motion during measurement.[42,43] The acquisition time for one B-scan image consisting of 2048 axis scans is at least 83 ms for the current SD-OCT. The axial motion of the eye can be at least 25 μm over this period,[42] which may add to the error for the measurement. As previous studies pointed out, the axial eye motion can be corrected or reduced by developing algorithms for postprocessing the image,[31] or applying the technique with ultra high speed imaging.[43,44]

In summary, we demonstrated a method for ocular surface shape measurement using the anterior segment SD-OCT. Algorithms were developed to automatically segment the ocular surface. The distortion caused by the nontelecentricity was calibrated and corrected. We also tested the accuracy and repeatability of the method. The development of this method may open a new era for studying the ocular surface in ophthalmic applications.

Acknowledgements

The authors wish to thank Britt Bromberg, PhD, Xenofile Editing, New Orleans, Louisiana, for providing editing services for this manuscript. This study was partially supported by research grants from Vistakon, NIH Center Grant No. P30 EY014801, and Research to Prevent Blindness (RPB).

References

1. D. Wasserman, J. Itzkowitz, T. Kamenar, and P. A. Asbell, "Corneal topographic data: its use in fitting aspheric contact lenses," *Contact Lens Association of Ophthalmologists Journal* **18**, 83–85 (1992).
2. B. E. McCarey, C. F. Amos, and L. R. Taub, "Surface topography of soft contact lenses for neutralizing corneal astigmatism," *Contact Lens Association of Ophthalmologists Journal* **19**, 114–120 (1993).
3. T. Reddy, L. B. Szczotka, and C. Roberts, "Peripheral corneal contour measured by topography influences soft toric contact lens fitting success," *Contact Lens Association of Ophthalmologists Journal* **26**, 180–185 (2000).
4. S. E. Wilson, D. T. Lin, and S. D. Klyce, "Corneal topography of keratoconus," *Cornea* **10**, 2–8 (1991).
5. R. A. Applegate, "Acuities through annular and central pupils after radial keratotomy," *Optom. Vision Sci.* **68**(8), 584–590 (1991).
6. B. Cense, N. Nassif, T. Chen, M. Pierce, S. H. Yun, B. Park, B. Bouma, G. Tearney, and J. F. de Boer, "Ultrahigh-resolution high-speed retinal imaging using spectral-domain optical coherence tomography," *Opt. Express* **12**, 2435–2447 (2004).
7. P. J. Caroline, M. P. Andre, and C. W. Norman, "Corneal topography and computerized contact lens-fitting modules," *International Contact Lens Clinic* **21**, 185–195 (1994).
8. K. L. Lim and H. B. Fam, "Relationship between the corneal surface and the anterior segment of the cornea: an Asian perspective," *J. Cataract Refractive Surg.* **32**(11), 1814–1819 (2006).
9. D. Z. Reinstein, R. C. Rothman, D. G. Couch, and T. J. Archer, "Artemis very high-frequency digital ultrasound-guided repositioning of a free cap after laser in situ keratomileusis," *J. Cataract Refractive Surg.* **32**(11), 1877–1883 (2006).
10. J. B. Ciolino and M. W. Belin, "Changes in the posterior cornea after laser in situ keratomileusis and photorefractive keratectomy," *J. Cataract Refractive Surg.* **32**(9), 1426–1431 (2006).
11. M. Dubbelman, V. A. Sicam, and G. L. Van Der Heijde, "The shape of the anterior and posterior surface of the aging human cornea," *Vision Res.* **46**(6–7), 993–1001 (2006).
12. S. A. Read, M. J. Collins, L. G. Carney, and R. J. Franklin, "The topography of the central and peripheral cornea," *Invest. Ophthalmol. Visual Sci.* **47**(4), 1404–1415 (2006).
13. D. Huang, E. A. Swanson, C. P. Lin, J. S. Schuman, W. G. Stinson, W. Chang, M. R. Hee, T. Flotte, K. Gregory, C. A. Puliafito, and J. G. Fujimoto. "Optical coherence tomography," *Science* **254**, 1178–1181 (1991).
14. J. A. Izatt, M. R. Hee, E. A. Swanson, C. P. Lin, D. Huang, J. S. Schuman, C. A. Puliafito, and J. G. Fujimoto, "Micrometer-scale resolution imaging of the anterior eye in vivo with optical coherence tomography," *Arch. Ophthalmol.* **112**(12), 1584–1589 (1994).
15. G. Hausler and M. W. Lindner, " 'Coherence Radar' and 'Spectral Radar'—new tools for dermatological diagnosis," *J.Biomed.Opt.* **3**, 21–31 (1998).
16. M. Wojtkowski, R. Leitgeb, A. Kowalczyk, T. Bajraszewski, and A. F. Fercher, "In vivo human retinal imaging by Fourier domain optical coherence tomography," *J. Biomed. Opt.* **7**, 457–463 (2002).
17. J. Jungwirth, B. Baumann, M. Pircher, E. Gotzinger, and C. K. Hitzenberger, "Extended in vivo anterior eye-segment imaging with full-range complex spectral domain optical coherence tomography," *J. Biomed. Opt.* **14**, 050501 (2009).
18. S. Fukuda, K. Kawana, Y. Yasuno, and T. Oshika, "Anterior ocular biometry using 3-dimensional optical coherence tomography," *Ophthalmology* **116**, 882–889 (2009).
19. M. Gora, K. Karnowski, M. Szkulmowski, B. J. Kaluzny, R. Huber, A. Kowalczyk, and M. Wojtkowski, "Ultra high-speed swept source OCT imaging of the anterior segment of human eye at 200 kHz with adjustable imaging range," *Opt. Express* **17**(17), 14880–14894 (2009).
20. B. Potsaid, B. Baumann, D. Huang, S. Barry, A. E. Cable, J. S. Schuman, J. S. Duker, and J. G. Fujimoto, "Ultrahigh speed 1050 nm swept source /Fourier domain OCT retinal and anterior segment imaging at 100,000 to 400,000 axial scans per second," *Opt. Express* **18**, 20029–20048 (2010).
21. R. Leitgeb, C. Hitzenberger, and A. Fercher, "Performance of fourier domain vs. time domain optical coherence tomography," *Opt. Express* **11**, 889–894 (2003).
22. J. F. de Boer, B. Cense, B. H. Park, M. C. Pierce, G. J. Tearney, and B. E. Bouma, "Improved signal-to-noise ratio in spectral-domain compared with time-domain optical coherence tomography," *Opt. Lett.* **28**, 2067–2069 (2003).

23. B. Park, M. C. Pierce, B. Cense, S. H. Yun, M. Mujat, G. Tearney, B. Bouma, and J. F. de Boer, "Real-time fiber-based multi-functional spectral-domain optical coherence tomography at 1.3 microm," *Opt. Express* **13**, 3931–3944 (2005).
24. Z. Wang, Z. Yuan, H. Wang, and Y. Pan, "Increasing the imaging depth of spectral-domain OCT by using interpixel shift technique," *Opt. Express* **14**, 7014–7023 (2006).
25. I. Grulkowski, M. Gora, M. Szkulmowski, I. Gorczynska, D. Szlag, S. Marcos, A. Kowalczyk, and M. Wojtkowski, "Anterior segment imaging with Spectral OCT system using a high-speed CMOS camera," *Opt. Express* **17**, 4842–4858 (2009).
26. T. Bajraszewski, M. Wojtkowski, M. Szkulmowski, A. Szkulmowska, R. Huber, and A. Kowalczyk, "Improved spectral optical coherence tomography using optical frequency comb," *Opt. Express* **16**, 4163–4176 (2008).
27. Z. Hu, Y. Pan, and A. M. Rollins, "Analytical model of spectrometer-based two-beam spectral interferometry," *Appl. Opt.* **46**, 8499–8505 (2007).
28. V. Westphal, A. Rollins, S. Radhakrishnan, and J. Izatt, "Correction of geometric and refractive image distortions in optical coherence tomography applying Fermat's principle," *Opt. Express* **10**, 397–404 (2002).
29. S. Ortiz, D. Siedlecki, L. Remon, and S. Marcos, "Optical coherence tomography for quantitative surface topography," *Appl. Opt.* **48**(35), 6708–6715 (2009).
30. S. Ortiz, D. Siedlecki, I. Grulkowski, L. Remon, D. Pascual, M. Wojtkowski and S. Marcos, "Optical distortion correction in optical coherence tomography for quantitative ocular anterior segment by three-dimensional imaging," *Opt. Express* **18**(3), 2782–2796 (2010).
31. M. Zhao, A. N. Kuo, and J. A. Izatt, "3D refraction correction and extraction of clinical parameters from spectral domain optical coherence tomography of the cornea," *Opt. Express* **18**(9), 8923–8936 (2010).
32. R. J. Zawadzki, C. Leisser, R. Leitgeb, M. Pircher, and A. F. Fercher, "Three-dimensional ophthalmic opticalcoherence tomography with a refraction correction algorithm," *Proc. SPIE* **5140**, 20–27 (2003).
33. M. V. Sarunic, S. Asrani, and J. A. Izatt, "Imaging the ocular anterior segment with real-time, full-range Fourier-domain optical coherence tomography," *Arch. Ophthalmol.* **126**(4), 537–542 (2008).
34. N. Otsu, "A threshold selection method from gray-level histograms," *IEEE Trans. Syst. Man. Cybern* **9**(1), 62–66 (1979).
35. M. Sonka, V. Hlavac, and R. Boyle, *Image Processing, Analysis, and Machine Vision*, 3rd ed., Thomson Learning, New York (2008).
36. B. R. Davidson and J. K. Barton, "Application of optical coherence tomography to automated contact lens metrology," *J. Biomed. Opt.* **15**(1), 016009 (2010).
37. S. A. Klein and R. B. Mandell, "Axial and instantaneous power conversion in corneal topography," *Invest. Ophthalmol. Visual Sci.* **36**, 2155–2159 (1995).
38. M. F. Chen and Y. P. Chen, "Compensating technique of field-distorting error for the CO2 laser galvanometric scanning drilling machines," *Int. J. Mach. Tools Manuf.* **47**(7–8), 1114–1124 (2007).
39. J. Xie, S. H. Huang, Z. C. Duan, Y. S. Shi, and S. F. Wen, "Correction of the image distortion for laser galvanometric scanning system," *Opt. Laser Technol.* **37**(4), 305–311 (2005).
40. M. Wojtkowski, A. Kowalczyk, R. Leitgeb, and A. F. Fercher, "Full range complex spectral optical coherence tomography technique in eye imaging," *Opt. Lett.* **27**, 1415–1417 (2002).
41. B. J. Vakoc, S. H. Yun, G. J. Tearney, and B. E. Bouma, "Elimination of depth degeneracy in optical frequency-domain imaging through polarization-based optical demodulation," *Opt. Lett.* **31**(3), 362–364 (2006).
42. M. Pircher, B. Baumann, E. Gotzinger, H. Sattmann, and C. K. Hitzenberger, "Simultaneous SLO/OCT imaging of the human retina with axial eye motion correction," *Opt. Express* **15**, 16922–16932 (2007).
43. B. Potsaid, I. Gorczynska, V. J. Srinivasan, Y. Chen, J. Jiang, A. Cable, and J. G. Fujimoto, "Ultrahigh speed spectral / Fourier domain OCT ophthalmic imaging at 70,000 to 312,500 axial scans per second," *Opt. Express* **16**, 15149–15169 (2008).
44. P. B. Morgan and N. Efron, "In vivo dehydration of silicone hydrogel contact lenses," *Eye Contact Lens* **29**, 173–176 (2003).